






RESEARCH ARTICLE

10.1029/2023JD038764

Albedo as a Competing Warming Effect of Urban Greening

Hannah L. Schlaerth¹ , Sam J. Silva^{1,2} , Yun Li¹, and Dan Li³ 

¹Department of Civil and Environmental Engineering, University of Southern California, Los Angeles, CA, USA,

²Department of Earth Sciences, University of Southern California, Los Angeles, CA, USA, ³Department of Earth and Environment, Boston University, Boston, MA, USA

Key Points:

- Increasing urban vegetation can reduce albedo, which increases incoming energy fluxes
- Albedo-induced effects of urban greening increased daytime 2-m air temperatures and suppressed most of the nighttime cooling signal
- Albedo-induced warming effects of urban greening may outweigh the cooling effects of increased evapotranspiration

Supporting Information:

Supporting Information may be found in the online version of this article.

Correspondence to:

H. L. Schlaerth,
hschlaer@usc.edu

Citation:

Schlaerth, H. L., Silva, S. J., Li, Y., & Li, D. (2023). Albedo as a competing warming effect of urban greening. *Journal of Geophysical Research: Atmospheres*, 128, e2023JD038764. <https://doi.org/10.1029/2023JD038764>

Received 23 FEB 2023
Accepted 21 NOV 2023

Author Contributions:

Conceptualization: Dan Li
Data curation: Yun Li
Formal analysis: Hannah L. Schlaerth
Investigation: Hannah L. Schlaerth
Methodology: Hannah L. Schlaerth
Resources: Sam J. Silva, Dan Li
Software: Yun Li
Supervision: Sam J. Silva, Dan Li
Validation: Hannah L. Schlaerth
Visualization: Hannah L. Schlaerth
Writing – original draft: Hannah L. Schlaerth
Writing – review & editing: Sam J. Silva, Yun Li, Dan Li

© 2023. The Authors.

This is an open access article under the terms of the [Creative Commons Attribution License](https://creativecommons.org/licenses/by/4.0/), which permits use, distribution and reproduction in any medium, provided the original work is properly cited.

Abstract Urban greening is often proposed for urban heat island (UHI) mitigation because vegetation provides shade and increases evapotranspiration. However, vegetation has lower albedo and higher emissivity than the bare soil it often replaces, which increases incoming energy fluxes. Here, we use the Weather Research and Forecasting model to quantify and compare the albedo and non-albedo effects (i.e., changes in emissivity, surface roughness, and evaporative fluxes) of urban greening in the Los Angeles Basin under policy relevant urban greening scenarios. When albedo-induced effects were included in the model, daytime surface temperatures in urban areas warmed by $0.70 \pm 0.89^\circ\text{C}$ with increases in the sensible heat flux outweighing increases in the latent heat flux from increased evapotranspiration. In contrast, daytime surface temperatures cooled by $0.27 \pm 0.72^\circ\text{C}$ when the albedo-induced effects were ignored. At night, including albedo-induced effects of urban greening resulted in only half the cooling modeled in the non-albedo simulations. Near surface air temperatures also had contrasting model results, with nighttime cooling of $0.21 \pm 0.47^\circ\text{C}$ outweighing slight daytime warming of $0.04 \pm 0.32^\circ\text{C}$ in the non-albedo simulations and daytime warming of $0.33 \pm 0.41^\circ\text{C}$ outweighing slight nighttime cooling of $0.05 \pm 0.46^\circ\text{C}$ in the albedo simulations. Our results reveal the critical role that albedo plays in determining the net surface climate effects of urban greening. Reductions in albedo from urban greening should be carefully considered by policy makers and urban planners, especially as high albedo roofs and pavements are simultaneously being deployed for UHI mitigation in many cities.

Plain Language Summary Urban greening initiatives are often proposed to cool cities because vegetation can provide shade and increase evaporative cooling. However, vegetation also has competing warming effects like decreasing albedo, meaning vegetation absorbs a larger fraction of incoming energy than the bare soil it often replaces. In this study, we used the Weather Research and Forecasting model to quantify and compare the effects of reduced albedo from urban greening to non-albedo effects, which included changes in emissivity, surface roughness, and evaporative fluxes. When reductions in albedo from urban greening were included in our model, daytime surface temperatures warmed by $0.70 \pm 0.89^\circ\text{C}$, indicating that the competing warming effects of urban greening outweighed the increased evaporative cooling from the added vegetation. In contrast, daytime surface temperatures cooled by $0.27 \pm 0.72^\circ\text{C}$ when reductions in albedo from urban greening were ignored. Our results reveal the critical role that albedo plays in determining the temperature effects of urban greening. Reductions in albedo from urban greening should be carefully considered by policy makers and urban planners to better optimize urban greening for heat mitigation, especially as cool surfaces like high albedo roofs and pavements are simultaneously being deployed in many cities.

1. Introduction

The urban heat island (UHI) effect describes the warmer temperatures observed in urban areas compared to their rural surroundings (Rosenfeld et al., 1998). Anthropogenic climate change will exacerbate the UHI effect and urbanization is rapidly increasing, making UHI mitigation of great public health interest to reduce heat exposure in densely populated urban areas (IPCC, 2023; United Nations, 2018).

The UHI effect is caused by the unique surface properties of urban areas, as is illustrated by comparing the surface energy balance of urban and rural land cover. The surface energy balance for an idealized control volume with no horizontal advection of heat can be expressed with Equation 1 (Oke et al., 2017; L. Wang and Li, 2021).

$$AH + (1 - \alpha)SW_{in} + \epsilon LW_{in} = SH + LH + G + \epsilon \sigma T_s^4 \quad (1)$$

where AH is the anthropogenic heat flux (W/m^2), α is albedo of the surface, SW_{in} is incoming shortwave radiation (W/m^2), ε is emissivity of the surface, LW_{in} is the incoming longwave radiation (W/m^2), SH is the sensible heat flux (W/m^2), LH is the latent heat flux (W/m^2), G is the ground heat flux (W/m^2), σ is the Stefan-Boltzmann constant ($\text{W/m}^2 \text{K}^4$) and T_s is the land surface temperature (K; L. Wang and Li, 2021). The left-hand side of Equation 1 represents incoming energy to the control volume whereas the right-hand side represents different pathways for energy transfer away from the control volume. In cities, the contribution of anthropogenic heat from buildings and cars as well as the presence of low albedo, thermally massive surfaces (i.e., low α and high ε values) results in a large flux of incoming energy. The abundance of impervious surface cover and the lack of vegetation makes water availability low in urban areas, shifting outgoing energy toward higher sensible heat fluxes and lower latent heat fluxes (Oke, 1982). As a result of these physical surface properties as well as the difference in the heat capacity of built versus natural land cover, urban areas experience warmer surface and near surface air temperatures relative to their rural surroundings (Oke, 1982).

UHI mitigation strategies aim to favorably shift the surface energy balance by changing the surface properties of urban areas. Urban greening and tree planting goals are increasingly proposed for UHI mitigation because plants increase evapotranspiration and provide shade, thereby increasing the latent heat flux and, in the case of shade, reducing incoming energy fluxes below the plant canopy (Rosenfeld et al., 1998). Urban greening also has the co-benefits of providing ecosystem services and reducing building energy use (Akbari, 2002; Akbari et al., 2001; Rosenfeld et al., 1998). While urban greening may increase evaporative fluxes, vegetation also has lower albedo and higher emissivity than the bare soil it often replaces, leading to larger net fluxes of shortwave and longwave radiation at the surface (Betts, 2000; Bonan, 2008). Moreover, vegetation also has enhanced surface roughness compared to bare land cover, which may reduce the cooling effects of wind on near surface air temperatures. Quantifying the competing warming and cooling effects of vegetation is critically important for optimizing urban greening for UHI mitigation.

Observational studies have offered clear consensus that areas shaded by vegetation are cooler than areas without shade (McGinn, 1982; Pincetl et al., 2013; Souch & Souch, 1993), but few have attempted to compare the relative contributions of shading and evapotranspiration from vegetation to the overall cooling observed (e.g., Pincetl et al., 2013) and none consider the competing warming effects of vegetation outlined above. Similarly, atmospheric modeling studies have focused on quantifying the cooling effects of urban greening, such as the effects of shading (Morakinyo et al., 2017; C. Wang et al., 2018) and evapotranspiration (X. X. Li & Liu, 2021), without considering the potential warming effects of changes to surface properties. Though studies like these provide valuable insight into the physical processes that contribute to cooling from vegetation, the competing warming effects of urban greening remain largely unquantified. Another limiting assumption of several previous works is that new vegetation would replace existing infrastructure such as urban land cover or lawns in urban greening scenarios, which leaves model results difficult to generalize to real world urban greening implementation (e.g., Fallmann et al., 2016; X. X. Li & Norford, 2016; Vahmani & Ban-Weiss, 2016b).

The albedo-induced effects of urban greening have yet to be considered in any prior modeling studies, but recent attention has been paid to the albedo-induced effects of global changes in vegetative land cover. Rohatyn et al. (2022) quantified the carbon sequestration potential of planting forests in drylands and compared it to the radiative forcing from accompanying changes in albedo in those areas. Their model results showed that the climate mitigation potential of forestation was low after accounting for albedo effects, only offsetting $\sim 1\%$ of carbon emissions under a business as usual emissions scenario (Rohatyn et al., 2022).

In the work presented here, we aim to address the literature gaps outlined above by quantifying and comparing the albedo-induced and non-albedo effects (e.g., emissivity, surface roughness, and changes to evaporative fluxes) of urban greening on surface climate using realistic, policy-driven scenarios. We used the Weather Research and Forecasting model (WRF) V3.7 with chemistry to simulate a 50% increase in urban vegetation in the Los Angeles Basin, an area with a long history of proposing urban greening initiatives (Pincetl et al., 2013). We quantified the response of albedo, evaporative fluxes, emissivity, and surface roughness to increased urban vegetation across the Los Angeles Basin in this realistic policy scenario. This work offers valuable insight for policy makers, urban planners, and regional modelers by demonstrating the critical role of albedo in determining the regional surface climate effects of urban greening.

2. Material and Methods

2.1. Model Description and Configuration

We simulate the response of the urban atmosphere to increasing vegetation using the WRF model V3.7 coupled to Chemistry (WRF-Chem) and the Single Layer Urban Canopy Model (SLUCM). Since the focus of this manuscript is on regional meteorology, information on chemistry schemes, chemical boundary conditions, and emissions data sets used can be found in the SI. Note that the results presented are not expected to be impacted by using WRF-Chem instead of the standalone version of WRF. The only drawback to using WRF-Chem for these simulations was increased computational time. The physics schemes used in the model were as follows: the Yonsei University Planetary Boundary Layer Scheme (Hong et al., 2006), the MM5 surface layer scheme (Dyer & Hicks, 1970; Paulson, 1970), the Lin et al. scheme for cloud microphysics (Lin et al., 1983), the rapid radiative transfer model longwave radiation scheme (Mlawer et al., 1997), the Goddard shortwave radiation scheme (Chou & Suarez, 1999), and the Grell 3D convective parameterization (Grell & Dévényi, 2002).

2.2. Simulation Domains

WRF uses two-way nested domains so that coarser, parent domains can be used as boundary conditions for the higher resolution, child domains that they contain. For the simulations presented in this work, three two-way nested domains were used with horizontal resolutions of 18, 6, and 2 km that were centered at 33.9°N, 118.14°W, as shown in Figure S1 of Supporting Information S1. Each domain had 29 unequally spaced, terrain-following vertical levels from the surface to 100 hPa. The North American Regional Reanalysis data set was used for initial and boundary meteorology conditions for all three domains (Mesinger et al., 2006).

2.3. Land Cover Data

Predicting the exchange of heat, momentum, and moisture between the land and atmosphere necessitates real world representation of land surface properties. Hence, we replaced WRF default values for several physical properties with real time remote sensing data (Vahmani and Ban-Weiss, 2016b). Input data for the green vegetation fraction (GVF), leaf area index, and albedo were derived from real-time satellite observations made by the MODerate resolution Imaging Spectroradiometer (MODIS) for the innermost domain. Raw data were retrieved from the United States Geological Society's Earth Explorer website and regridded to the innermost domain following Vahmani and Ban-Weiss (2016a).

Landcover was categorized using the National Land Cover Database (NLCD) from 2006 for all three domains. This 33-category land classification data set categorizes urban areas as low-intensity residential, high-intensity residential, and industrial/commercial (Fry et al., 2011). Whereas the default version of the SLUCM uses predefined urban fraction values for each urban category, we replaced default values with gridded urban fraction data for the innermost domain using the 2006 NLCD imperviousness data set (Wickham et al., 2013) following Vahmani and Ban-Weiss (2016a). Note that the 2006 NLCD imperviousness data set may slightly underestimate impervious land cover for 2012 due to urban development during this timeframe. When available, a gridded data set of urban morphology parameters (e.g., building heights, road widths, and roof widths) was created with the National Urban Database and Access Portal Tool (NUDAPTS; Ching et al., 2009). Where NUDAPTS data were unavailable, average building and road morphology for each of the aforementioned NLCD urban categories was used from the Los Angeles Region Imagery Acquisition Consortium, as was done in Zhang et al. (2018). Lastly, we used an irrigation module tuned for Southern California that simulates irrigation three times a week at 23:00 PST in the pervious fraction of urban grid cell by prescribing soil moisture to equal 28% (Vahmani and Hogue, 2014).

2.4. Single Layer Urban Canopy Model

In WRF, urban grid cells are divided into pervious and impervious land cover, the latter of which is referred to as the urban fraction. For the urban fraction of grid cells, WRF uses the Single Layer Urban Canopy Model (SLUCM; Chen et al., 2011; Kusaka et al., 2012; Yang et al., 2015) to calculate the surface energy balance between urban surfaces and the atmosphere. The SLUCM accounts for the radiative effects of the geometry of urban areas (i.e., shading from buildings, reflection off canyon walls, and trapped radiation) and includes

Table 1
Vegetation Parameters Used for Urban Grid Cells in the Noah Land Surface Model

Vegetation category	Min. emissivity	Max. emissivity	Min. roughness length (m)	Max. roughness length (m)
Urban vegetation	0.93	0.97	0.14	0.34
Urban and built-up land	0.88	0.88	0.50	0.50

anthropogenic heat fluxes. The remaining pervious fraction of urban grid cells is composed of bare soil and vegetation. Our configuration of WRF includes an added land cover category called Urban Vegetation for vegetative land cover in the pervious fraction of urban grid cells. Note that soil types for all three domains are from the National Center of Atmospheric Research in a data set derived from 30-s data from the State Soil Geographic Database.

2.5. Noah Land Surface Model

The Noah Land Surface Model (LSM) is used to calculate the surface energy balance for pervious land cover in urban grid cells and for all non-urban grid cells. GVF, defined here as the fraction of pervious land cover that is vegetation, is a key parameter in the Noah LSM. Our model code is modified to convert pixel-level GVF to the GVF of the pervious fraction of urban grid cells, hereafter referred to as the pervious-level GVF and described in Vahmani and Ban-Weiss (2016b). GVF is used in the Noah LSM to partition total evaporation between direct evaporation from bare soil and evaporation from the plant canopy (e.g., through transpiration or evaporation of intercepted precipitation; Chen & Dudhia, 2001). Seasonal variability in GVF is used to scale several other land surface parameters that include roughness length, emissivity, and albedo. Roughness length and emissivity are scaled proportionally with increasing GVF using Equation 2:

$$\text{VEGPARM} = \left(1 - \frac{\text{GVF}}{\text{GVF}_{\max} - \text{GVF}_{\min}}\right) \text{VEGPARM}_{\min} + \frac{\text{GVF}}{\text{GVF}_{\max} - \text{GVF}_{\min}} \text{VEGPARM}_{\max} \quad (2)$$

where VEGPARM is the calculated parameter value used in WRF, GVF is the current GVF, GVF_{\min} , and GVF_{\max} are gridded data sets of the yearly minimum and maximum GVF, and VEGPARM_{\min} and VEGPARM_{\max} are minimum and maximum values of roughness length or emissivity for each land cover category. The minimum and maximum parameter values for urban land cover are shown in Table 1. For urban vegetation, we used parameter values from Vahmani and Ban-Weiss (2016b). These parameter values represent two-thirds mixed forest and one-third grass lawns, which reflects typical urban landscaping in the Los Angeles area (McPherson et al., 2008).

In the default Noah LSM, albedo is scaled inversely with increasing GVF using Equation 3:

$$\text{Albedo} = \left(1 - \frac{\text{GVF}}{\text{GVF}_{\max} - \text{GVF}_{\min}}\right) \text{albedo}_{\max} + \frac{\text{GVF}}{\text{GVF}_{\max} - \text{GVF}_{\min}} \text{albedo}_{\min} \quad (3)$$

where Albedo is the calculated albedo used in WRF in the absence of gridded, real-time albedo data and albedo_{\min} and albedo_{\max} are the yearly minimum and maximum albedo values for each land cover category, respectively.

The Noah LSM has a few shortcomings that should be noted when interpreting the results of this study. First, the Noah LSM does not include the effects of shade from trees when calculating surface temperatures of pervious landcover and only includes effects from shade when calculating evaporative fluxes from bare soil. Thus, the diagnostic 2 m air and surface temperatures discussed in the results reflect the temperature above the plant canopy and the temperature of the vegetated surface, respectively, rather than temperatures below the plant canopy (e.g., Vahmani and Ban-Weiss, 2016a). Additionally, by treating the urban and pervious fractions separately, potential interactions between urban landcover and vegetation are not resolved. In particular, the effect of increased vegetation on roughness length may be overestimated since buildings would dominate surface friction in urban areas. Moreover, this modeling framework does not allow us to explore potential effects of adding vegetation to the urban fraction of model grid cells. Additionally, pixel-level albedo values are used to calculate the surface energy balance for sub pixel-level land cover, which may not accurately reflect the individual albedo of pervious and impervious landcover. Future work is needed to improve the representation of heterogeneous land cover in regional atmospheric models.

2.6. Simulation Design

To quantify and compare the albedo-induced and non-albedo effects of urban greening, we designed two sets of simulations that are summarized in Table 2 and described here. The first set of simulations are the GVF50

Table 2
Summary of Simulations

Simulation name	GVF	Albedo	Mean albedo in urban grid cells
Baseline	MODIS	MODIS	0.11 ± 0.03
GVF50	$1.5 \times \text{MODIS}$	MODIS	0.11 ± 0.03
Baseline_Albedo	MODIS	Noah LSM	0.18 ± 0.05 Min. albedo: 0.18 Max. albedo: 0.24
GVF50_Low_Albedo	$1.5 \times \text{MODIS}$	Noah LSM	0.12 ± 0.04 Min. albedo: 0.18 Max. albedo: 0.24
GVF50_High_Albedo	$1.5 \times \text{MODIS}$	Noah LSM	0.12 ± 0.05 Min. albedo: 0.23 Max. albedo: 0.24

and Baseline simulations, which we hereafter referred to as the non-albedo simulations. The Baseline scenario used the MODIS-derived GVF described above to represent the baseline land cover. For the urban greening scenario, GVF50, the existing pervious-level GVF in urban grid cells was increased by a relative change of 50%, as depicted schematically in Figure S2a of Supporting Information S1. In contrast, urban greening scenarios used in previous work (e.g., Fallmann et al., 2016; X. X. Li & Norford, 2016) replace existing urban land cover with vegetation similar to the illustration in Figure S2b of Supporting Information S1. In the rare instance where increasing GVF by 50% would surpass the total pervious fraction of grid cells, the pervious-level GVF was set to 100%, meaning new vegetation never replaced existing urban land cover. In GVF50 and Baseline, we turned off the option in the Noah LSM that scales albedo with the seasonal variation in GVF and instead used the gridded MODIS albedo described above for both simulations, which is shown in Figure S3a of Supporting Information S1. Hence, changes between GVF50 and Baseline reflect only the non-albedo effects (i.e., changes to emissivity, roughness length, and evaporative fluxes) of urban greening.

The second simulation set includes Baseline_Albedo, GVF50_Low_Albedo, and GVF50_High_Albedo, which are referred to as the albedo simulations.

For the albedo simulations, we turned on the option in the Noah LSM that adjusts albedo proportionally with seasonal variations in GVF. Accordingly, the albedo simulations include albedo-induced effects in addition to the non-albedo effects of urban greening. The Baseline_Albedo simulation used the MODIS-derived GVF (i.e., the GVF used in Baseline) to establish a baseline for the Noah-calculated albedo against which the GVF50_Low_Albedo and GVF50_High_Albedo simulations could be directly compared. This was necessary since the albedo simulations have somewhat different albedo values in both urban and nonurban areas compared to the non-albedo simulations since the former used the Noah LSM to calculate albedo throughout the entire domain whereas the latter used measured albedo values, as shown in Figure S3 of Supporting Information S1. In the GVF50_Low_Albedo and GVF50_High_Albedo simulations, the pervious-level GVF was increased by 50% in urban grid cells, as was done in GVF50. Then, albedo was correspondingly scaled by the Noah LSM using Equation 3. In GVF50_Low_Albedo, we used the default albedo_{min} and albedo_{max} look-up table values of 0.18 and 0.24, which reflect seasonal minima and maxima in albedo. The differences between the default Albedo_{min} and Albedo_{max} values was 0.06, which is similar to the difference between the MODIS derived albedo for grid cells in our study area composed primarily of vegetation (mean albedo = 0.11) and those composed primarily of bare soil (mean albedo = 0.18). We tested the sensitivity of our model results to potential parametric errors in the albedo calculation in the Noah LSM in GVF50_High_Albedo. Here, we increased the Albedo_{min} look-up table value, which is weighed more heavily in the albedo calculation as GVF increases (see Equation 3), to reflect a smaller difference in albedo between bare soil and the new vegetation replacing it. We chose an Albedo_{min} look-up table value of 0.23 in GVF50_High_Albedo, which reflects a change in albedo of 0.01 between seasonal maxima and minima albedo values. This change in albedo is similar to observations reported by Rose and Levinson (2013) for dry, bare soil converted to dry vegetation and may be more representative of summer albedo values compared to GVF50_Low_Albedo.

Note that the model scenarios explored in this study do not cover all potential albedo outcomes from urban greening, but instead represent upper and lower bounds for a policy realistic urban greening implementation where vegetation has replaced bare soil. Net albedo effects depend on both the albedo of the vegetation added as well as the albedo of the surface being replaced. Though unlikely, an urban greening implementation where high albedo vegetation replaces low albedo urban surfaces (e.g., freshly paved roads) could potentially increase albedo in certain areas. For both the albedo and non-albedo simulations, we assumed no additional irrigation would be needed to sustain the newly planted vegetation given the already water stressed region and made no changes to the irrigation scheme used in the urban greening scenarios. Since our irrigation scheme simulates irrigation in the pervious fraction of urban grid cells (i.e., soil moisture is prescribed for both bare soil and vegetation), our simulation design instead represents a significant shift in the allocation of total evaporation. This transition moves the landscape away from being predominantly dominated by evaporation from bare soil, and instead, promotes evapotranspiration through the plant canopy. We ran our simulations from 1 July 2012 00:00 through 31 July 2012 23:00 LST to represent a typical summer month and employed a 5-day model spin-up.

3. Results

3.1. Model Validation

We assessed model performance by comparing the Baseline simulation against hourly observations of 2 m air temperature data from the network of Air Quality System (AQS) maintained by the US EPA (2012). AQS data were obtained from 25 measurement stations located throughout the innermost domain (US EPA (2012) Air Quality Systems Data Mart). Their locations are presented in Figure S4 of Supporting Information S1. We compared hourly model outputs to hourly 2 m air temperature data from the Baseline simulation in Figure S5a of Supporting Information S1. We spatially averaged the hourly AQS data and compared it against the average of the WRF grid cells that contained AQS stations in Figure S5b of Supporting Information S1. The 2 m air temperature from the Baseline simulation was strongly correlated with observations ($r = 0.91$). The model tends to underestimate 2 m air temperature relative to observations, with a mean error of 2.1 K and a mean bias of 0.4 K. This model performance is consistent with previous studies that have used similar model configurations in the same study area (Y. Li et al., 2019; Vahmani & Ban-Weiss, 2016a, 2016b; Zhang et al., 2018). A comparison of model statistics and recommended model benchmarks is presented in Table S1 of Supporting Information S1.

We also compared land surface temperatures predicted by WRF against MODIS daytime surface temperatures from the MOD11A1 version 6.1 data product (Wan et al., 2021). The MOD11A1 data product provides daytime surface temperature data with daily temporal resolution and 1-km horizontal resolution based on remote sensing measurements made by MODIS. Data availability was limited by cloud cover and quality assurance issues during our simulation period, so we limited our analysis to time periods with high MODIS data coverage. We found that mean daytime land surface temperature predicted by WRF was 307.8 K and the mean from MODIS was 308.3 K, the correlation between the two data sources was reasonably high ($r = 0.51$, see Figure S6 in Supporting Information S1). These results are consistent with the model performance reported in L. Wang and Li (2021), which used a similar model configuration. Given that MODIS errors can be large over spatially heterogeneous surfaces as in urban regions (e.g., Duan et al., 2019), we believe that the similar mean surface temperature and relatively high correlation support the use of WRF for sensitivity studies presented here. However, future work investigating the bias between WRF simulations and MODIS surface temperature retrievals would be beneficial.

3.2. Changes to Physical Surface Properties From Urban Greening

Figure 1 shows surface properties for the baseline landcover and the changes in those properties from increasing GVF in the urban greening scenarios, GVF50, GVF50_Low_Albedo, and GVF50_High_Albedo. The mean \pm standard deviation of the GVF in urban grid cells was $33.4 \pm 12.7\%$ for Baseline and Baseline_Albedo (Figure 1a). Since the urban greening scenarios employed a relative increase in pervious-level GVF, the increase in GVF was spatially heterogeneous. Following a 50% relative increase in GVF, the mean GVF increased by $16.6 \pm 6.23\%$ in the urban greening scenarios, shown in Figure 1b.

Increasing GVF considerably decreased albedo in both the GVF50_Low_Albedo and GVF50_High_Albedo simulations relative to the Baseline_Albedo simulation, as shown in Figures 1c and 1d. For urban grid cells in the Baseline_Albedo simulation, the mean \pm standard deviation of albedo calculated by the Noah LSM was 0.18 ± 0.05 . Albedo decreased on average by 0.06 ± 0.03 and 0.06 ± 0.04 in the GVF50_Low_Albedo and GVF50_High_Albedo simulations, respectively. Our estimated decrease in albedo from urban greening is within the range estimated by Rose and Levinson (2013), a remote sensing study that quantified changes in albedo following increased vegetation in neighborhoods in Sacramento and Los Angeles, CA. Though the albedo_{min} value for urban vegetation increased considerably in the GVF50_High_Albedo simulation, there was practically no change compared to the albedo calculated for the GVF50_Low_Albedo simulation (Figure S3 in Supporting Information S1), indicating that the calculated albedo is more sensitive to the large increase in GVF as opposed to the lookup table albedo values.

Figures 1e and 1f shows the roughness length for baseline landcover and the change in roughness length for the urban greening scenarios. Increasing GVF by 50% increased roughness length considerably in urban grid cells. The mean increase was 0.11 ± 0.05 m in the urban greening simulations, which corresponded to a relative increase of 42.3% compared to the roughness length of the baseline land cover. Increasing GVF did not cause as large a change to emissivity, as shown in Figures 1g and 1h. The mean increase in emissivity for urban grid cells was 0.03 ± 0.01 in the urban greening simulations, which was a relative increase of 2.8%.

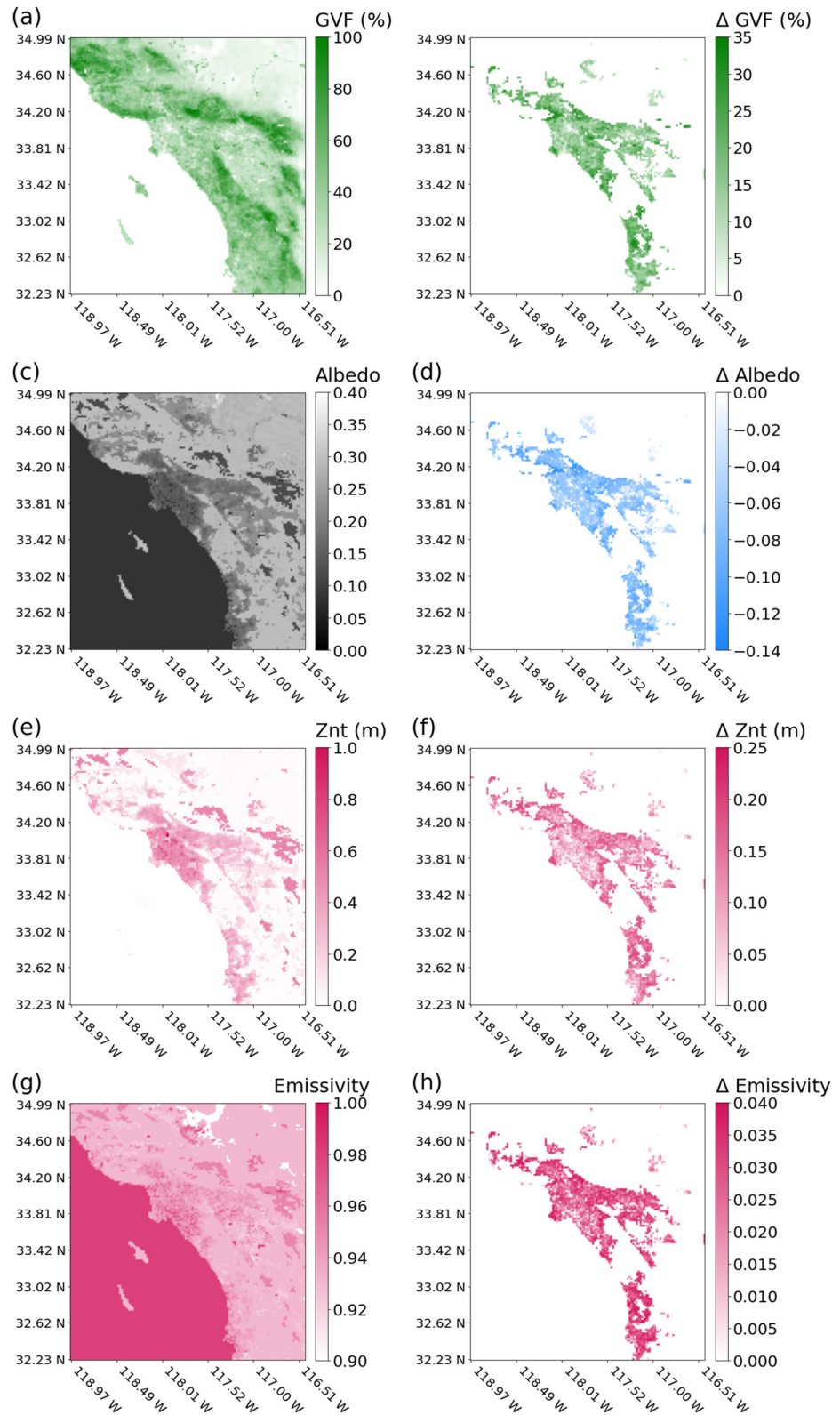


Figure 1. Surface properties for baseline land cover (left column) and changes in those properties from increasing urban vegetation (right column). Note that panel (c) shows the albedo calculated by Weather Research and Forecast for the Baseline_Albedo simulation and Panel (d) shows the change in albedo between the GVF50_Low_Albedo and the Baseline_Albedo simulations. The change in albedo between GVF50_High_Albedo and Baseline_Albedo is nearly identical to that shown in Panel (d) and is shown in Figure S3 in Supporting Information S1.

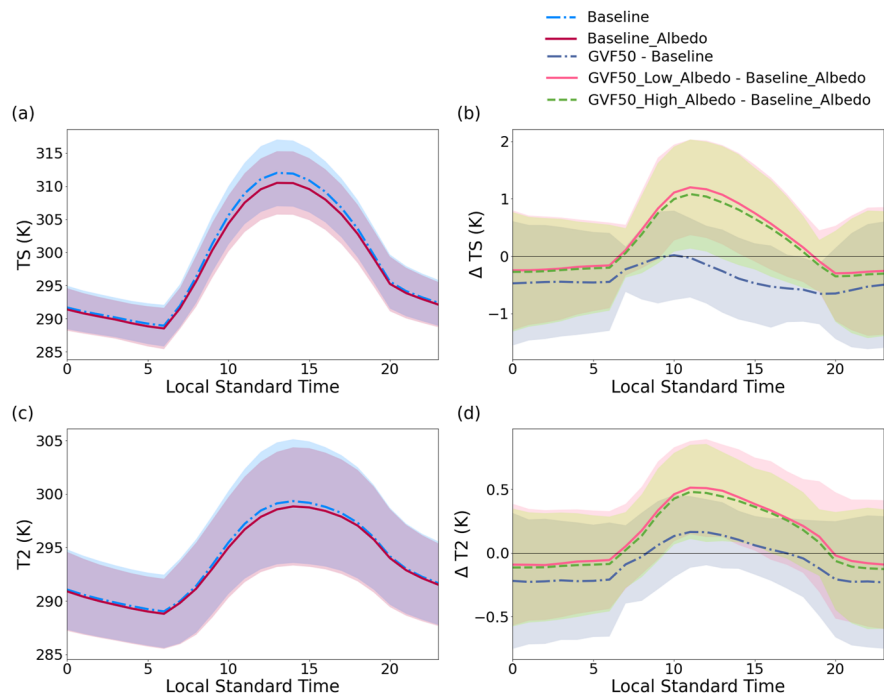


Figure 2. Panel (a) shows spatially-averaged diurnal cycle of surface temperature (TS) in urban grid cells for the baseline simulations and Panel (b) shows the change in surface temperature for the increased green vegetation fraction simulations compared to their respective baselines. Panels (c and d) are the same as Panels (a and b) but for 2 m air temperature (T2). Shading denotes the standard deviation, which reflects both spatial and temporal variability.

3.3. Changes in Land Surface and Near Surface Air Temperatures

The baseline and changes in diurnal cycles of surface and near surface air temperature in urban grid cells are shown in Figure 2. Here we discuss the mean daytime (06:00–19:00 LST) and nighttime (20:00–05:00 LST) temperature changes, which were spatially averaged over all urban grid cells. Note that the standard deviations reported here reflect both temporal and spatial variability. Accounting for the albedo effects of urban greening changed the direction of the daytime surface temperature signal and reduced the magnitude of the nighttime cooling signal, as shown in Figures 2a and 2b. When albedo was left unchanged in GVF50, mean daytime surface temperature cooled by 0.27 ± 0.72 K urban grid cells. Including the albedo-induced effects of increasing GVF led to warmer mean daytime surface temperatures of 0.70 ± 0.89 and 0.61 ± 0.93 K in urban grid cells in GVF50_Low_Albedo and GVF50_High_Albedo, respectively. Nighttime surface temperature cooled in urban grid cells by 0.52 ± 0.94 K in GVF50. The large standard deviations of these surface temperature results are partly due to the spatial heterogeneity of changes in GVF in the urban greening simulations. We used a two-tailed *t*-test and found that the surface temperature signals in urban grid cells were statistically significant under a 95% confidence interval for all of our urban greening simulations compared to their respective baselines.

Figures 2c and 2d illustrate the average diurnal cycle of 2 m air temperature in urban grid cells for the suite of simulations. Including albedo-induced effects resulted in daytime 2 m air temperature warming of 0.33 ± 0.41 K and 0.29 ± 0.38 K in urban grid cells in GVF50_Low_Albedo and GVF50_High_Albedo, respectively. Although surface temperature slightly cooled when albedo-induced effects were neglected, daytime 2 m air temperature had a slight warming signal during the day of 0.04 ± 0.32 K in urban grid cells in GVF50. This daytime warming is consistent with the effect of increased surface roughness reducing wind speeds (Figure S7 in Supporting Information S1), resulting in less turbulent transport of warm, near surface air compared to the baseline scenario. At night, a strong cooling signal of 0.21 ± 0.47 K was modeled in urban grid cells when albedo-induced effects were neglected in GVF50. In comparison, the albedo simulations had a reduced nighttime cooling signal by more than 50% with mean nighttime surface cooling of 0.23 ± 0.91 K in GVF50_Low_Albedo and cooling of 0.27 ± 0.90 K in GVF50_High_Albedo. The reduction in nighttime cooling indicates that the warming effects from reducing albedo somewhat counteracted the nighttime cooling effects of urban greening. We used a two-tailed *t*-test and

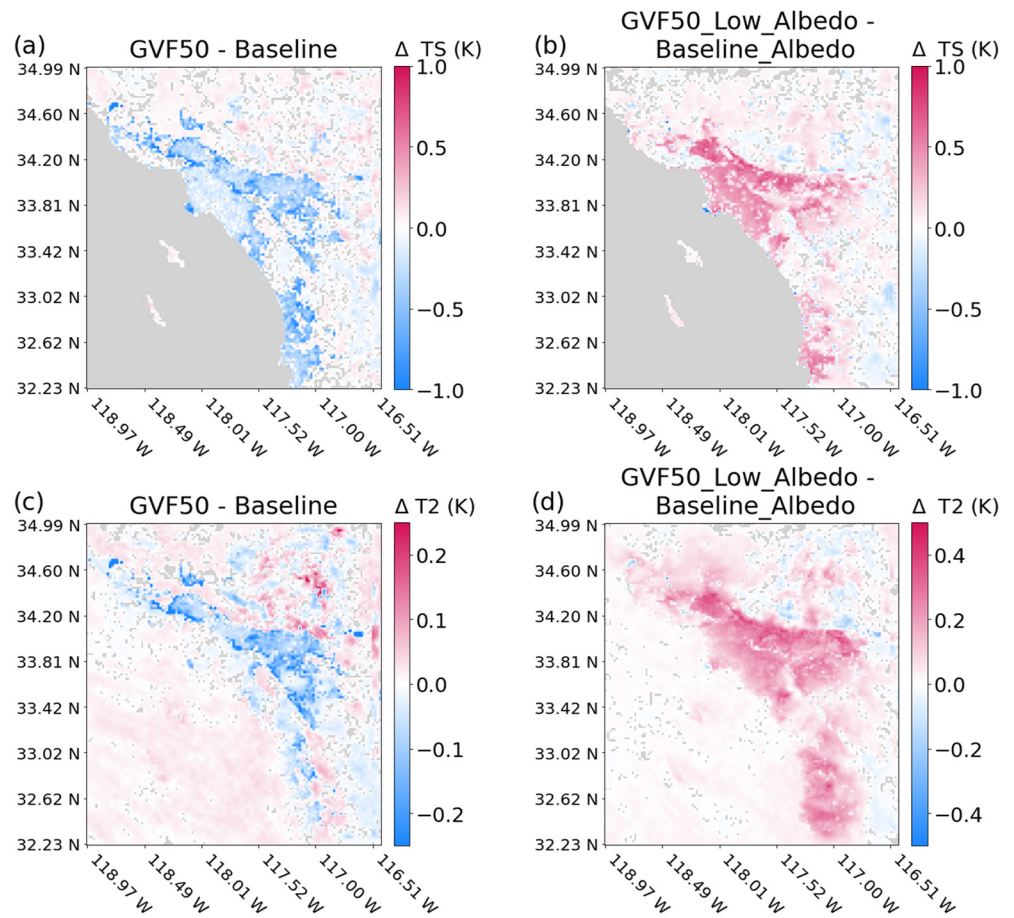


Figure 3. The average daily change in (a and b) surface temperature and the average daily change in 2 m (c and d) air temperature. Areas shown in gray were not statistically distinguishable from zero under a 95% confidence interval. Results for GVF50_High_Albedo are shown in Figure S8 of Supporting Information S1.

found that the 2 m air temperature signals in urban grid cells were statistically significant under a 95% confidence interval for all of our urban greening simulations compared to their respective baselines.

Figure 3 shows the spatial distribution of changes in the daily mean surface temperature and 2 m air temperature for the urban greening scenarios compared to their baselines. We used a two-tailed *t*-test with a 95% confidence interval and show only statistically significant changes in daily average temperatures in the data presented in Figure 3. Changes in surface temperature, shown in Figures 3a and 3b, were constrained to urban areas and visually comparable in magnitude to the spatial distribution of increased GVF shown in Figure 1a for both GVF50 and GVF50_Low_Albedo. Surface temperature changes corresponded to small 2 m air temperature changes in the albedo and non-albedo simulations, as shown in Figures 3c and 3d. While changes in 2 m air temperature followed roughly the same spatial pattern as changes in surface temperature for the GVF50 simulation, the 2 m air temperature warming modeled in the GVF50_Low_Albedo simulation extended to some areas outside of the urban grid cells. Notably, including the albedo-induced effects of urban greening in GVF50_Low_Albedo reversed the mean daily surface and near surface air temperature signals in most urban grid cells. A cooling signal was modeled in several grid cells in Long Beach, indicating that enhanced evapotranspiration outweighed the albedo-induced effects of urban greening in this small region.

3.4. Changes in Energy Fluxes

Figure 4 shows the spatially averaged diurnal cycles of the incoming and outgoing energy terms from Equation 1 for urban grid cells with the diurnal cycles for the energetic contribution of net shortwave and longwave fluxes shown in Figures 4a–4d. The net shortwave fluxes shown in Figure 4a are different for Baseline and

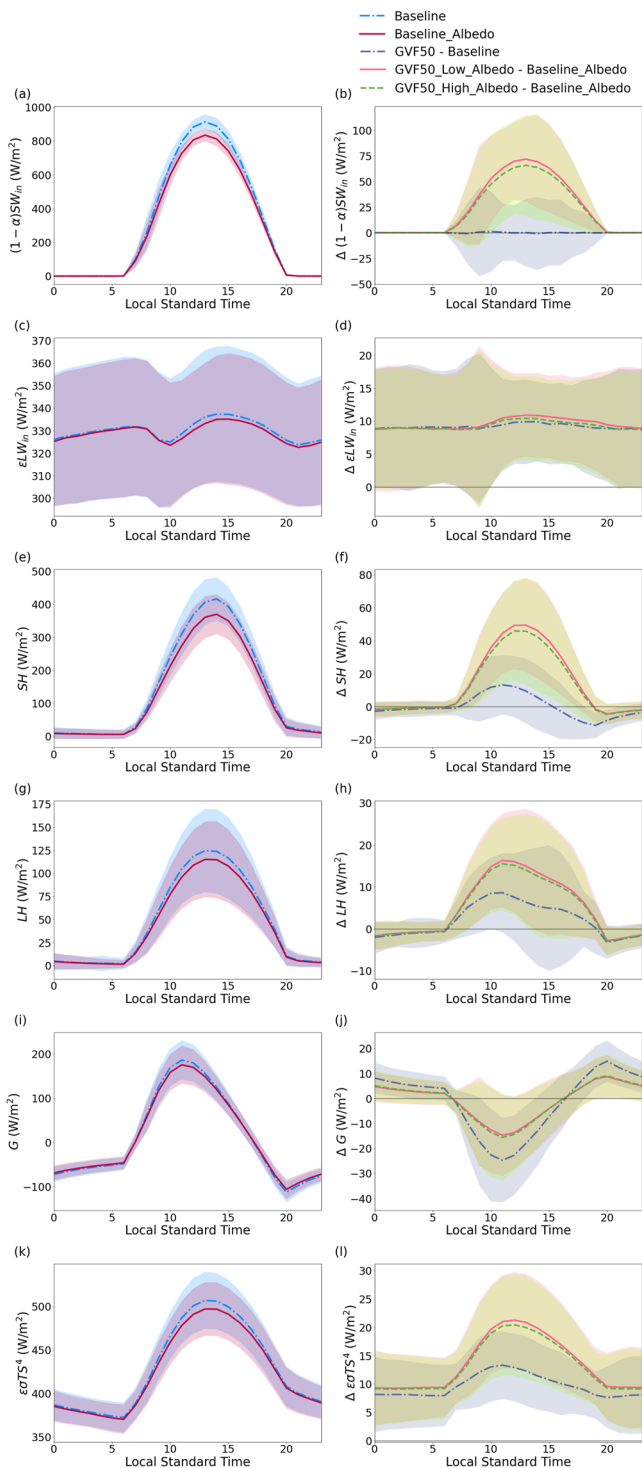


Figure 4. (a–d) The spatially averaged diurnal cycles of the incoming and (e–l) outgoing energy terms from Equation 1 for urban grid cells. Panels on the left represent diurnal cycles of energy fluxes for baseline land cover and panels on the right are changes in energy fluxes modeled in the urban greening simulations compared to their respective baselines. Shading denotes the standard deviation.

Baseline_Albedo since the former used gridded observational albedo data and the latter calculated albedo values based on GVF using Equation 3 (see Figure S3 in Supporting Information S1). In the albedo simulations, albedo decreased with increased GVF resulting in increased net shortwave radiation. The mean \pm standard deviation of the daytime change in the net shortwave flux for GVF50_Low_Albedo and GVF50_High_Albedo was 41.01 ± 42.88 and 38.5 ± 44.82 W/m^2 respectively. Note that the wide standard deviation reflects the spatial heterogeneity of the albedo-induced effects since GVF was increased by a relative percent. In contrast, GVF50 had almost no change in the shortwave flux compared to the baseline simulation. Small variations modeled during daytime hours are consistent with slight changes in scattered shortwave radiation by aerosols between GVF50 and Baseline. Incoming longwave fluxes changed slightly between the baseline and urban greening simulations, as shown in Figures 4c and 4d. During the day, incoming longwave fluxes increased by 9.28 ± 7.88 , 9.90 ± 8.07 , and 9.58 ± 7.95 W/m^2 in the GVF50, GVF50_Low_Albedo and GVF50_High_Albedo simulations compared to their respective baselines (Figure 4d). At night, incoming longwave fluxes similarly increased by 8.94 ± 9.04 , 8.99 ± 9.13 , and 8.86 ± 8.87 W/m^2 for each respective simulation (Figure 4d). The incoming longwave fluxes are similar for the albedo and non-albedo simulations because the incoming longwave flux is more sensitive to changes in emissivity rather than changes in albedo, which is consistent with Equation 1.

Figures 4e–4h depict the spatially averaged diurnal cycles of sensible and latent heat fluxes, which are the first two outgoing energy terms on the right-hand side of Equation 1. The sensible heat flux increased only slightly during the day in GVF50 compared to Baseline with a mean daytime increase in urban grid cells of 2.96 ± 16.55 W/m^2 . In comparison, the sensible heat flux increased by nearly an order of magnitude more in GVF50_Low_Albedo and GVF50_High_Albedo, with mean daytime changes of 25.62 ± 27.44 and 23.46 ± 28.35 W/m^2 , respectively. Note that the standard deviation can be large given the spatial heterogeneity of increased GVF and the month-long simulation length. At night, the albedo and non-albedo simulations had slightly lower sensible heat fluxes compared to their respective baselines with average nighttime change for urban grid cells of -3.61 ± 5.71 , -2.02 ± 5.06 , and -2.10 ± 4.99 W/m^2 , for GVF50, GVF50_Low_Albedo, and GVF50_High Albedo, respectively.

Increasing GVF changed evaporative fluxes in urban grid cells and is reflected by changes in the latent heat flux as shown in Figures 4g and 4h. During the day, latent heat fluxes increased slightly in the GVF50 simulation compared to the Baseline simulation with a mean change of 4.62 ± 10.20 W/m^2 . Daytime latent heat fluxes increased by approximately twice that modeled in GVF50, with GVF50_Low_Albedo increasing by 9.63 ± 11.63 W/m^2 and GVF50_High_Albedo by 9.09 ± 11.38 W/m^2 compared to Baseline_Albedo. The increased daytime latent heat fluxes in the albedo and non-albedo simulations reflect increased evapotranspiration from added vegetation. The albedo simulations had higher increases in the latent heat fluxes due to the additional effect of increased near surface air temperatures, which promote evapotranspiration and direct evaporation from bare soil. At night, total evaporation is dominated by evaporation from bare soil since vegetation is treated as photosynthetically inactive with closed stomata. Since the urban greening simulations had less landcover made up of bare soil, nighttime latent heat

fluxes decreased. The average nighttime changes were -1.87 ± 5.71 W/m² in GVF50, -1.59 ± 5.06 W/m² in GVF50_Low_Albedo, and -1.65 ± 4.99 W/m² in GVF50_High_Albedo.

Figures 4i–4l show the baseline and changes to the diurnal cycles of the ground heat flux and the outgoing longwave radiation flux from the right-hand side of Equation 1. The GVF50 simulation had minimal changes in surface temperature during the day and only a small increase in emissivity, resulting in a slight daytime increase of 10.76 ± 5.78 W/m² in outgoing longwave radiation compared to Baseline, as shown in Figures 4k and 4l. The albedo simulations experienced increased surface temperatures and correspondingly had higher increases in outgoing longwave radiation during the day, with average daytime increases of 16.27 ± 9.37 and 15.73 ± 9.16 W/m², respectively. Though surface temperature cooled at night in GVF50, the increased emissivity from increasing GVF led to slightly increased outgoing longwave radiation with an average increase of 5.78 ± 6.22 W/m² in urban grid cells. In the albedo simulations, nighttime surface temperatures decreased less than in the GVF50 simulation, resulting in larger increases in outgoing longwave radiation of 8.22 ± 6.37 W/m² in GVF50_Low_Albedo and 8.31 ± 6.32 W/m² in GVF50_High_Albedo.

During the day, energy is transferred from the atmosphere to ground storage through conduction, shown as a positive ground flux in Figure 4i. Less energy was transferred to ground storage in GVF50 compared to Baseline during daytime hours, with an average daytime change of -8.55 ± 16.73 W/m² in urban grid cells. Smaller decreases were modeled in the albedo simulations, with average changes of -4.90 ± 13.50 and -5.19 ± 8.31 W/m² in the GVF50_Low_Albedo and GVF50_High_Albedo, respectively (Figure 4j). Again, note that the large variability can be attributed in part to the spatial heterogeneity of increased GVF in the region. At night, energy is released to the atmosphere from ground storage which is represented as a negative flux in Figure 4i. The change in the nighttime ground storage terms for the albedo and non-albedo simulations were approximately equal in magnitude and opposite in direction to their corresponding daytime changes described above (Figure 4j).

4. Discussion

Urban greening is one of the most often proposed methods of UHI mitigation, yet little work has been done to quantify the competing warming effects of increased vegetative cover on surface climate. In particular, no prior work has considered the albedo-induced effects of urban greening on surface climate. Understanding the competing warming effect of urban greening, like that of reduced albedo, is critically important for optimizing urban greening implementation for UHI mitigation.

In this study, we used WRF-Chem to simulate realistic, policy-driven urban greening scenarios and quantified the albedo-induced and non-albedo effects (e.g., changes in surface roughness, emissivity, and evaporative fluxes) of urban greening in the Los Angeles Basin. Our model results showed that accounting for the albedo-induced effects of urban greening changed the direction of the daytime surface temperature signal and suppressed nighttime cooling. Interestingly, in both the albedo and non-albedo simulations, changes in surface temperature corresponded to only slight changes in 2 m air temperature despite the large increase in GVF.

The unintuitive daytime surface temperature warming modeled in the albedo simulations is made clear when compared to the changes in the incoming and outgoing energy flux terms from Equation 1. In the albedo simulations, the reduced albedo from urban greening led to large increases in the net shortwave flux and increases in the sensible heat flux that outweighed increases in the latent heat flux, resulting in daytime surface temperature warming up to 0.70 ± 0.89 K in GVF50_Low_Albedo. In contrast, neglecting the albedo effects in the non-albedo simulation led to increased latent heat fluxes that outweighed increases in the sensible heat flux, resulting in cooler mean daytime surface temperatures in urban areas by 0.27 ± 0.72 K.

Our temperature results are consistent with findings from Pincetl et al. (2013), who analyzed remote sensing data and found that irrigated grass lawns in Los Angeles, CA did not reduce surface temperatures, suggesting that evapotranspiration did not contribute significantly to cooling from vegetation (Pincetl et al., 2013). However, prior regional modeling studies on urban greening predict more cooling than was modeled in both the albedo and non-albedo simulations. Beyond differing model configurations, one likely cause for the discrepancy is the different urban greening implementation scenarios between our studies. Fallmann et al. (2016) and X. X. Li and Norford (2016) used urban greening scenarios where vegetation replaced urban land cover and report more near surface air cooling than was modeled in our non-albedo simulation. In contrast, our urban greening scenarios assumed that new urban vegetation would only replace bare soil and

hence, we made no changes to the impervious fraction of urban grid cells. Our results therefore isolate the role of increased vegetation in a manner that better aligns with how cities will realistically increase vegetated land.

Our model results point to important directions for future work. First, our temperature results showed that the albedo-induced effects of urban greening outweighed cooling from increased evapotranspiration during the day, but fully capturing the net temperature effects of urban greening requires a better representation of heterogeneous land cover in urban areas. As described in the methodology, WRF by default calculates the surface energy balance separately for pervious and impervious land cover, which means that our model results do not capture several important radiative effects of urban greening, such as shading of pavement from street trees or the trapping of outgoing longwave radiation from increased canopy cover. Recent work has made progress improving the representation of temperatures below the plant canopy and within urban canyons (e.g., Lee et al., 2016; Morakinyo et al., 2017; C. Wang et al., 2018), but more work is needed to elucidate how the albedo-induced effects of vegetation explored in the current study play into the complex radiative effects of urban tree planting.

Our model results also show that large regional increases in urban vegetation have the potential to reduce albedo, which needs to be considered as cities are simultaneously implementing high albedo roofs and pavements for UHI mitigation. As an illustrative example, Ko et al. (2022) measured the albedo of a pilot scale implementation of high albedo pavement in a neighborhood in Covina, CA and measured an increase in albedo compared to pre installation ranging from 0.08 to 0.26. In comparison, the 50% increase in vegetation in our study corresponded to a mean decrease in albedo of 0.06 ± 0.03 in GVF50_Low_Albedo. The extent to which decreases in albedo from urban greening may counteract increases in albedo from high albedo roofs and pavements needs to be quantified in future work.

5. Conclusion

In the work presented here, we used WRF-Chem to quantify the response of albedo, evaporative fluxes, emissivity, and surface roughness to a 50% increase in urban vegetation across the Los Angeles Basin under a realistic urban greening scenario. We analyzed our model results in the context of the surface energy balance by looking at changes in incoming and outgoing energy fluxes from the albedo-induced and non-albedo effects of urban greening. This work is the first to consider changes in albedo from urban greening.

The contrasting daytime temperature results between the albedo and non-albedo simulations and the reduced nighttime cooling signal in the albedo simulations highlight the critical importance of constraining the role of albedo when assessing the net effects of urban greening on the surface energy balance. The daytime surface warming signal in the albedo simulations suggests that more irrigation may be needed to outweigh the competing warming effects of urban greening, which may not be realistic in water stressed regions like Southern California. Moreover, the dampened nighttime cooling signal in the albedo simulations may indicate that previous modeling studies overestimated cooling from urban greening. These albedo-induced effects of urban greening need to be carefully considered in future modeling studies and more work is needed to investigate temperature effects below the plant canopy. Reductions in albedo from urban greening should also be carefully considered by policy makers and urban planners, especially as cool surfaces like high albedo roofs and pavements are simultaneously being deployed for UHI mitigation in many cities.

Conflict of Interest

The authors declare no conflicts of interest relevant to this study.

Data Availability Statement

Model inputs, output data and Jupyter Notebook scripts used to produce the figures presented in the main text and supporting information are preserved at Zenodo (Schlaerth, 2023). Air temperature data used to validate model performance are available for download at the US EPA (2012) Data Mart. Data analysis and visualization were conducted in Python version 3.0.

Acknowledgments

This work was supported by the National Science Foundation Graduate Research Fellowship under Grant DGE-1842487. Any opinion, findings, and conclusions or recommendations expressed in this material are those of the author(s) and do not necessarily reflect the views of the sponsors. An extension of gratitude to the late George Ban-Weiss for advising this project in its early stages.

References

Akbari, H. (2002). Shade trees reduce building energy use and CO₂ emissions from power plants. *Environmental Pollution*, 116, S119–S126. [https://doi.org/10.1016/s0269-7491\(01\)00264-0](https://doi.org/10.1016/s0269-7491(01)00264-0)

Akbari, H., Pomerantz, M., & Taha, H. (2001). Cool surfaces and shade trees to reduce energy use and improve air quality in urban areas. *Solar Energy*, 70(3), 295–310. [https://doi.org/10.1016/S0038-092X\(00\)00089-X](https://doi.org/10.1016/S0038-092X(00)00089-X)

Betts, R. A. (2000). Offset of the potential carbon sink from boreal forestation by decreases in surface albedo. *Nature*, 408(6809), 187–190. <https://doi.org/10.1038/35041545>

Bonan, G. B. (2008). Forests and climate change: Forcings, feedbacks, and the climate benefits of forests. *Science*, 320(5882), 1444–1449. <https://doi.org/10.1126/science.1155121>

Chen, F., & Dudhia, J. (2001). Coupling an advanced land surface–hydrology model with the Penn State–NCAR MM5 modeling system. Part I: Model implementation and sensitivity. *Monthly Weather Review*, 129(4), 569–585. [https://doi.org/10.1175/1520-0493\(2001\)129<0569:caalsh>2.0.co;2](https://doi.org/10.1175/1520-0493(2001)129<0569:caalsh>2.0.co;2)

Chen, F., Kusaka, H., Bornstein, R., Ching, J., Grimmond, C. S. B., Grossman-Clarke, S., et al. (2011). The integrated WRF/urban modelling system: Development, evaluation, and applications to urban environmental problems. *International Journal of Climatology*, 31(2), 273–288. <https://doi.org/10.1002/joc.2158>

Ching, J., Brown, M., Burian, S., Chen, F., Cionco, R., Hanna, A., et al. (2009). National urban database and access portal tool. *Bulletin of the American Meteorological Society*, 90(8), 1157–1168. <https://doi.org/10.1175/2009bams2675.1>

Chou, M.-D., & Suarez, M. J. (1999). Technical Report Series on Global Modeling and Data Assimilation. In *A Solar Radiation Parameterization for Atmospheric Studies* (Vol. 15, pp. 11–38). Goddard Space Flight Center.

Duan, S. B., Li, Z. L., Li, H., Göttsche, F. M., Wu, H., Zhao, W., et al. (2019). Validation of Collection 6 MODIS land surface temperature product using in situ measurements. *Remote Sensing of Environment*, 225, 16–29. <https://doi.org/10.1016/j.rse.2019.02.020>

Dyer, A. J., & Hicks, B. B. (1970). Flux-gradient relationships in the constant flux layer. *Quarterly Journal of the Royal Meteorological Society*, 96(410), 715–721. <https://doi.org/10.1002/qj.49709641012>

Fallmann, J., Forkel, R., & Emeis, S. (2016). Secondary effects of urban heat island mitigation measures on air quality. *Atmospheric Environment*, 125, 199–211. <https://doi.org/10.1016/j.atmosenv.2015.10.094>

Fry, J. A., Xian, G., Jin, S. M., Dewitz, J. A., Homer, C. G., Yang, L. M., et al. (2011). Completion of the 2006 national land cover database for the conterminous United States. *Photogrammetric Engineering & Remote Sensing*, 77(9), 858–864.

Grell, G. A., & Dévényi, D. (2002). A generalized approach to parameterizing convection combining ensemble and data assimilation techniques. *Geophysical Research Letters*, 29(14), 38-1–38-4. <https://doi.org/10.1029/2002gl015311>

Hong, S. Y., Noh, Y., & Dudhia, J. (2006). A new vertical diffusion package with an explicit treatment of entrainment processes. *Monthly Weather Review*, 134(9), 2318–2341. <https://doi.org/10.1017/9781139016476>

IPCC. (2023). In Core Writing Team, H. Lee, & J. Romero (Eds.), *Climate Change 2023: Synthesis Report. Contribution of Working Groups I, II and III to the Sixth Assessment Report of the Intergovernmental Panel on Climate Change* (pp. 35–115). IPCC. <https://doi.org/10.59327/IPCC/AR6-9789291691647>

Ko, J., Schlaerth, H., Bruce, A., Sanders, K., & Ban-Weiss, G. (2022). Measuring the impacts of a real-world neighborhood-scale cool pavement deployment on albedo and temperatures in Los Angeles. *Environmental Research Letters*, 17(4), 044027. <https://doi.org/10.1088/1748-9326/ac58a8>

Kusaka, H., Chen, F., Tewari, M., Dudhia, J., Gill, D. O., Duda, M. G., et al. (2012). Numerical simulation of urban heat island effect by the WRF model with 4-km grid increment: An inter-comparison study between the urban canopy model and slab model. *Journal of the Meteorological Society of Japan. Ser. II*, 90B(0), 33–45. <https://doi.org/10.2151/jmsj.2012-b03>

Lee, S. H., Lee, H., Park, S. B., Woo, J. W., Lee, D. I., & Baik, J. J. (2016). Impacts of in-canyon vegetation and canyon aspect ratio on the thermal environment of street canyons: Numerical investigation using a coupled WRF-VUCM model. *Quarterly Journal of the Royal Meteorological Society*, 142(699), 2562–2578. <https://doi.org/10.1002/qj.2847>

Li, X. X., & Liu, X. (2021). Effect of tree evapotranspiration and hydrological processes on urban microclimate in a tropical city: A WRF/SLUCM study. *Urban Climate*, 40, 101009. <https://doi.org/10.1016/j.uclim.2021.101009>

Li, X. X., & Norford, L. K. (2016). Evaluation of cool roof and vegetations in mitigating urban heat island in a tropical city, Singapore. *Urban Climate*, 16, 59–74. <https://doi.org/10.1016/j.uclim.2015.12.002>

Li, Y., Zhang, J., Sailor, D. J., & Ban-Weiss, G. A. (2019). Effects of urbanization on regional meteorology and air quality in Southern California. *Atmospheric Chemistry and Physics*, 19(7), 4439–4457. <https://doi.org/10.5194/acp-19-4439-2019>

Lin, Y. L., Farley, R. D., & Orville, H. D. (1983). Bulk parameterization of the snow field in a cloud model. *Journal of Applied Meteorology and Climatology*, 22(6), 1065–1092. [https://doi.org/10.1175/1520-0450\(1983\)022<1065:bpotsf>2.0.co;2](https://doi.org/10.1175/1520-0450(1983)022<1065:bpotsf>2.0.co;2)

Meginn, C. E. (1982). *The microclimate and energy use in suburban tree canopies (California)*. ProQuest Dissertations Publishing.

McPherson, E. G., Simpson, J. R., Xiao, Q., & Chunxia, W. (2008). *Los Angeles 1-Million tree canopy cover assessment. General Technical Report PSW-GTR-207* (p. 52). U.S. Department of Agriculture, Forest Service, Pacific Southwest Research Station.

Mesinger, F., DiMego, G., Kalnay, E., Mitchell, K., Shafran, P. C., Ebisuzaki, W., et al. (2006). North American regional reanalysis. *Bulletin of the American Meteorological Society*, 87(3), 343–360. <https://doi.org/10.1175/bams-87-3-343>

Mlawer, E. J., Taubman, S. J., Brown, P. D., Iacono, M. J., & Clough, S. A. (1997). Radiative transfer for inhomogeneous atmospheres: RRTM, a validated correlated-k model for the longwave. *Journal of Geophysical Research*, 102(D14), 16663–16682. <https://doi.org/10.1029/97jd00237>

Morakinyo, T. E., Kong, L., Lau, K. K. L., Yuan, C., & Ng, E. (2017). A study on the impact of shadow-cast and tree species on in-canyon and neighborhood's thermal comfort. *Building and Environment*, 115, 1–17. <https://doi.org/10.1016/j.buildenv.2017.01.005>

Oke, T. R. (1982). The energetic basis of the urban heat island. *Quarterly Journal of the Royal Meteorological Society*, 108(455), 1–24. <https://doi.org/10.1002/qj.49710845502>

Oke, T. R., Mills, G., Christen, A., & Voogt, J. A. (2017). *Urban climates*. Cambridge University Press.

Paulson, C. A. (1970). The mathematical representation of wind speed and temperature profiles in the unstable atmospheric surface layer. *Journal of Applied Meteorology and Climatology*, 9(6), 857–861. [https://doi.org/10.1175/1520-0450\(1970\)009<0857:tmrows>2.0.co;2](https://doi.org/10.1175/1520-0450(1970)009<0857:tmrows>2.0.co;2)

Pincetl, S., Gillespie, T., Pataki, D. E., Saatchi, S., & Saphores, J. D. (2013). Urban tree planting programs, function or fashion? Los Angeles and urban tree planting campaigns. *Geojournal*, 78(3), 475–493. <https://doi.org/10.1007/s10708-012-9446-x>

Rohatyn, S., Yakir, D., Rotenberg, E., & Carmel, Y. (2022). Limited climate change mitigation potential through forestation of the vast dryland regions. *Science*, 377(6613), 1436–1439. <https://doi.org/10.1126/science.abm9684>

Rose, L. S., & Levinson, R. (2013). Analysis of the effect of vegetation on albedo in residential areas: Case studies in suburban Sacramento and Los Angeles, CA. *GIScience and Remote Sensing*, 50(1), 64–77. <https://doi.org/10.1080/15481603.2013.778557>

- Rosenfeld, A. H., Akbari, H., Romm, J. J., & Pomerantz, M. (1998). Cool communities: Strategies for heat island mitigation and smog reduction. *Energy and Buildings*, 28(1), 51–62. [https://doi.org/10.1016/s0378-7788\(97\)00063-7](https://doi.org/10.1016/s0378-7788(97)00063-7)
- Schlaerth, H. (2023). Albedo as a competing warming effect of urban greening [Dataset]. Zenodo. Retrieved from <https://zenodo.org/records/10035646>
- Souch, C. A., & Souch, C. (1993). The effect of trees on summertime below canopy urban climates: A case study Bloomington, Indiana. *Journal of Arboriculture*, 19(5), 303–312. <https://doi.org/10.48044/jauf.1993.049>
- United Nations. (2018). World urbanization prospects: The 2018 revision: Key facts. Retrieved from population.un.org/wup/Publications/Files/WUP2018-KeyFacts.pdf
- US EPA. (2012). Air Quality System Data Mart [Dataset]. US EPA. Retrieved from https://aqs.epa.gov/aqswb/airdata/download_files.html
- Vahmani, P., & Ban-Weiss, G. (2016a). Climatic consequences of adopting drought-tolerant vegetation over Los Angeles as a response to California drought. *Geophysical Research Letters*, 43(15), 8240–8249. <https://doi.org/10.1002/2016gl069658>
- Vahmani, P., & Ban-Weiss, G. A. (2016b). Impact of remotely sensed albedo and vegetation fraction on simulation of urban climate in WRF-urban canopy model: A case study of the urban heat island in Los Angeles. *Journal of Geophysical Research: Atmospheres*, 121(4), 1511–1531. <https://doi.org/10.1002/2015jd023718>
- Vahmani, P., & Hogue, T. S. (2014). Incorporating an urban irrigation module into the Noah land surface model coupled with an urban canopy model. *Journal of Hydrometeorology*, 15(4), 1440–1456. <https://doi.org/10.1175/jhm-d-13-0121.1>
- Wan, Z., Hook, S., & Hulley, G. (2021). MODIS/Terra Land Surface Temperature/Emissivity Daily L3 Global 1km SIN Grid V061 [Dataset]. NASA EOSDIS Land Processes Distributed Active Archive Center. <https://doi.org/10.5067/MODIS/MOD11A1.061>
- Wang, C., Wang, Z. H., & Yang, J. (2018). Cooling effect of urban trees on the built environment of contiguous United States. *Earth's Future*, 6(8), 1066–1081. <https://doi.org/10.1029/2018EF000891>
- Wang, L., & Li, D. (2021). Urban heat islands during heat waves: A comparative study between Boston and Phoenix. *Journal of Applied Meteorology and Climatology*, 60(5), 621–641. <https://doi.org/10.1175/JAMC-D-20-0132.1>
- Wickham, J. D., Stehman, S. V., Gass, L., Dewitz, J., Fry, J. A., & Wade, T. G. (2013). Accuracy assessment of NLCD 2006 land cover and impervious surface. *Remote Sensing of Environment*, 130, 294–304. <https://doi.org/10.1016/j.rse.2012.12.001>
- Yang, J., Wang, Z. H., Chen, F., Miao, S., Tewari, M., Voegt, J. A., & Myint, S. (2015). Enhancing hydrologic modelling in the coupled weather research and forecasting–urban modelling system. *Boundary-Layer Meteorology*, 155(1), 87–109. <https://doi.org/10.1007/s10546-014-9991-6>
- Zhang, J., Mohegh, A., Li, Y., Levinson, R., & Ban-Weiss, G. (2018). Systematic comparison of the influence of cool wall versus cool roof adoption on urban climate in the Los Angeles Basin. *Environmental Science & Technology*, 52(19), 11188–11197. <https://doi.org/10.1021/acs.est.8b00732>

References From the Supporting Information

- Ackermann, I. J., Hass, H., Memmesheimer, M., Ebel, A., Binkowski, F. S., & Shankar, U. M. A. (1998). Modal aerosol dynamics model for Europe: Development and first applications. *Atmospheric Environment*, 32(17), 2981–2999. [https://doi.org/10.1016/s1352-2310\(98\)00006-5](https://doi.org/10.1016/s1352-2310(98)00006-5)
- Ahmadov, R., McKeen, S. A., Robinson, A. L., Bahreini, R., Middlebrook, A. M., De Gouw, J. A., et al. (2012). A volatility basis set model for summertime secondary organic aerosols over the eastern United States in 2006. *Journal of Geophysical Research*, 117(D6), D06301. <https://doi.org/10.1029/2011jd016831>
- CARB. (2017). *ARB's emission inventory activities*. California Air Resources Board. Retrieved from [ww2.arb.ca.gov/emission-inventory-activities#:~:text=An emission inventory is an, in a calendar year](http://ww2.arb.ca.gov/emission-inventory-activities#:~:text=An%20emission%20inventory%20is%20an%20,calendar%20year)
- Emery, C., Liu, Z., Russell, A. G., Odman, M. T., Yarwood, G., & Kumar, N. (2017). Recommendations on statistics and benchmarks to assess photochemical model performance. *Journal of the Air & Waste Management Association*, 67(5), 582–598. <https://doi.org/10.1080/10962247.2016.1265027>
- Emmons, L. K., Walters, S., Hess, P. G., Lamarque, J. F., Pfister, G. G., Fillmore, D., et al. (2010). Description and evaluation of the Model for Ozone and Related chemical Tracers, version 4 (MOZART-4). *Geoscientific Model Development*, 3(1), 43–67. <https://doi.org/10.5194/gmd-3-43-2010>
- Guenther, A., Karl, T., Harley, P., Wiedinmyer, C., Palmer, P. I., & Geron, C. (2006). Estimates of global terrestrial isoprene emissions using MEGAN (Model of emissions of Gases and Aerosols from Nature). *Atmospheric Chemistry and Physics*, 6(11), 3181–3210. <https://doi.org/10.5194/acp-6-3181-2006>
- Kim, S. W., Heckel, A., Frost, G. J., Richter, A., Gleason, J., Burrows, J. P., et al. (2009). NO₂ columns in the western United States observed from space and simulated by a regional chemistry model and their implications for NO_x emissions. *Journal of Geophysical Research*, 114(D11), D11301. <https://doi.org/10.1029/2008jd011343>
- Madronich, S. (1987). Photodissociation in the atmosphere: 1. Actinic flux and the effects of ground reflections and clouds. *Journal of Geophysical Research*, 92(D8), 9740–9752. <https://doi.org/10.1029/jd092id08p09740>
- US EPA. (2014). *Previous NEI Reports*. US EPA. Retrieved from www.epa.gov/air-emissions-inventories/previous-nei-reports